



Modeling of continuum robots with environmental constraints

Peng Chen^{1,2,3} · Yuwang Liu^{1,2} · Tingwen Yuan^{1,2,4} · Wenping Shi^{1,2,4}

Received: 20 January 2022 / Accepted: 6 June 2023 / Published online: 27 June 2023
© The Author(s), under exclusive licence to Springer-Verlag London Ltd., part of Springer Nature 2023

Abstract

Leveraging the intrinsic compliance of continuum robots is a promising approach to enable symbiosis and harmoniousness in an unstructured environment. This compliance in interaction reduces the risk of damage for both the robot and its surroundings. However, the high degrees of freedom of continuum robots complicates the establishment of an analytical model that accurately describes the robot mechanical behavior, particularly in the case of large deformations during contact with obstacles. In this study, a novel modeling method is explored and the configuration space parameters of a robot are defined by considering the environmental constraints and variable curvature. A 10-section continuum robot prototype with a length of 1 m, was developed to validate the model. The robot's ability to reach the target points, to follow complex paths and incidents of contacting with obstacles validate the feasibility and accuracy of the model. The ratio of the robot endpoint average position errors to its length are 2.045% and 2.446%, respectively, in conditions without and with obstacle. Thus, this work may serve as a reference for designing and analyzing continuum robots, providing a new perspective on the integration of robots with the environment.

Keywords Environmental constraints · Obstacle contact · Soft continuum robot · Variable-curvature model

1 Introduction

Owing to their inherent high flexibility, excellent adaptability and natural and safe interoperability, continuum robots are receiving increasing attention in the fields of medical care [1], manipulation [2], rescue [3], inspection [4] and wearable devices [5], among others, demonstrating significant development potential [6, 7]. The rapid evolution of this technology has led to new solutions and bright prospects in the areas of safety and flexibility, which poses difficult challenges for the traditional robots operating in complex environments [8, 9]. However, the high degrees of freedom and the acting internal and external forces, still complicate

the establishment of a computationally accurate and efficient kinematics model [10, 11].

Examples of continuum robot actuator modules include flexible driven rods [12–14] and pneumatic actuators [15–17]. Unlike the traditional rigid-link robots, the elasticity should actually be considered in the modeling of a continuum robot. Static analysis is carried out, instead of kinematics, in order to accurately describe the occurring deformation [18]. Desired spatial curves are described using mathematical methods, and fitting continuum robots to these curves as closely as possible. [19, 20]. The current modeling methods are mainly based on constant curvature [21] and variable curvature approaches [22].

The constant curvature approach is a simplified perception, also called the piecewise constant curvature method [14, 23]. According to this approach, a series of tangent arcs is used to approximate the configuration of the continuum robot [24]. The advantages of a simple model and easy solution make the constant curvature method widely used in the field of continuum robot modeling [25]. Based on this method, Robert et al. [26] and Rucker et al. [27] established a kinematic model of a concentric tube continuum robot, which could predict the robot deformation. Escande et al. [28] developed a model for a soft manipulator and

✉ Yuwang Liu
liuyuwang@sia.cn

¹ State Key Laboratory of Robotics, Shenyang Institute of Automation, Chinese Academy of Sciences, Shenyang, China

² Institutes for Robotics and Intelligent Manufacturing, Chinese Academy of Sciences, Shenyang, China

³ University of Chinese Academy of Sciences, Beijing, China

⁴ School of Mechanical Engineering and Automation, Northeastern University, Shenyang, China

proposed two experimental setups, in order to conduct model calibration and validation. Gong et al. [29] combined computer vision and proposed a kinematic modeling method for a three-degree-of-freedom continuum robot, grasping sea cucumbers underwater. Yang et al. [30] developed a model of a continuum robot with adjustable stiffness and analyzed the deformation of the robot under external forces.

Variable curvature approaches have also been developed, to serve in cases where the constant curvature approach is not suitable, such as when the local curvature changes greatly. Godage et al. [31] proposed a novel model for continuum robots based on mode shape functions (MSFs), which can predict robot bending very well. Gonthina et al. [32] proposed a model based on Euler spiral curve and proved the superiority of their approach, compared to the constant curvature approach. Singh et al. [33] described a model based on Pythagorean hodograph (PH) curves, which can obtain the bending deformation of continuum robot in the three-dimensional space. Bieze et al. [34] presented a model based on the finite element method, which can perform forward and inverse kinematics analysis of a soft continuum robot. Huang et al. [35] considered the external forces and proposed a model based on the absolute nodal coordinates formulation. The aforementioned approaches considered the kinematics of the robot body and the influence of the load, describing the kinematics more precisely; however, they did not consider the robot-obstacle interaction.

In future applications of continuum robots, the interaction with the environment needs to be considered [36, 37], since they are susceptible to gravity and to obstacles in unstructured operating environments. Therefore, a continuum robot model should not only consider the ontology, but also focus on the influence and constraints introduced by the obstacle. The occurrence of an obstacle contact during path planning results in the advantage that it limits the uncertainty of motion [38, 39], but it also poses certain difficulties in the theoretical modeling approach. Some scholars have considered the modeling of continuum robots operating in a constrained environment. Zhang et al. [40] developed a contact model of a cable-driven continuum robot with obstacle while bending in a two-dimensional plane, which can calculate the contact force of the robot without the need of force sensor. Yip et al. [41] achieved the first model-free control method based on the interaction between a continuum robot and constrained environment. Chen et al. [42] proposed a 1-DOF pneumatic soft robot modelling method for contact detection and contact position estimation, and the algorithm was able to successfully estimate the contact position. Della Santina et al. [43] considered the impact of environmental constraints on the robot endpoint moving in a two-dimensional space. They proposed an alternative formula for the dynamics of robots and introduced two control frameworks to achieve more accurate curvature control. Greer et al.

[44] studied the obstacle avoidance problem in the case of continuum robots operating in a chaotic environment. They exploited the contact to avoid obstacle when it was beneficial for navigation. However, continuum robots inevitably encounter situations, wherein they need to bypass obstacles, while operating in a three-dimensional space. Moreover, existing modeling methods are ineffective in solving this problem, thus motivating for the present study.

This work investigated a continuum robot variable curvature modeling method, which considered environmental constraints. At first, an unconstrained continuum robot model with boundary conditions was established. Next, a model with obstacle constraint was established, by describing the robot-obstacle contact occurrence using an inequality function. Based on the least squares method, the solution of equations system was converted into a constrained nonlinear optimization problem. The Lagrange multiplier method and Levenberg–Marquardt (LM) algorithm were used to solve the model. The configurations of the continuum robot were obtained by interpolation and fitting the discrete nodes. A novel 10-section continuum robot prototype, driven by origami airbags, was developed, along with the design of a control system. The theoretical model was verified experimentally.

This paper is organized as follows: in Sect. 2, a quasi-static model of a continuum robot is established and the solution method is introduced. Section 3 describes the development of a continuum robot prototype with 10 sections, driven by origami airbags, used in three sets of experiments, in order to verify the proposed model. Finally, the conclusion is presented in Sect. 4.

2 Modeling

2.1 Main model

A continuum robot driven by origami airbags (OAs) generally consists of several sections, which is composed of two constraint disks and three OAs, which are juxtaposed in each section apart, as shown in Fig. 1. The backbone, which is located at the center of the constraint disk, typically uses an elastic rod. The working principle of the drive OAs is that the working length can be changed, so the structure with telescopic function can be used as a drive actuator. The configuration of the backbone can be used as the configuration of the robot because the structure of the robot has a symmetric distribution.

As depicted in Fig. 2, a continuum robot is discretized into n elements, and N_i represents the i th nodes. The spindle coordinate system of N_i is $N_i - x_i y_i z_i$. The gravitational force of the robot is f_g , and the contact force $f_{c,i}$ are applied at N_i . The position vector of N_i in the inertial

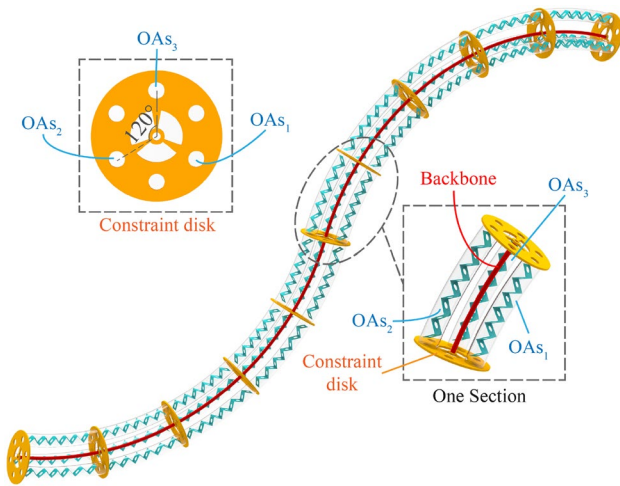


Fig. 1 Generalized structure of continuum robot driven by OAs

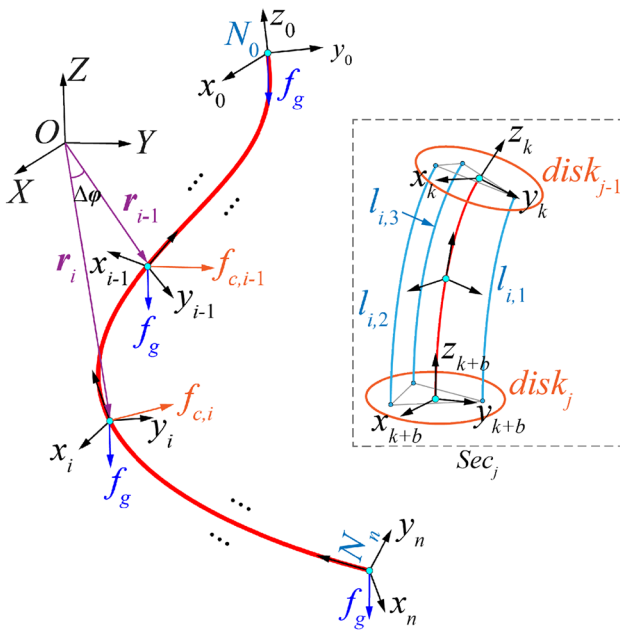


Fig. 2 Geometric schematic view used to describe a continuum robot

coordinate system $O - XYZ$ is r_i . The sectional angular displacement is defined as $\Delta\varphi$. The robot length between N_{i-1} and N_i is l_r , $l_r = L/n$, where L denotes the length of the robot. There are m constraint disks, where the section between $disk_{i-1}$ and $disk_i$ is called Sec_i . Evidently, there are b ($b = n/m$) nodes in Sec_i . The length of OA_j in Sec_i is $l_{i,j}$.

The configuration of the robot can be determined from the pose matrix R and the position vector r of these nodes. The arc coordinates are designated as s , $s \in [0, L]$. Let

$$Q = \begin{bmatrix} R & r \\ 0 & 1 \end{bmatrix}. \tag{1}$$

The advantages of quaternions to avoid singular solutions are more suitable for numerical calculations [45]. Therefore, R can be represented by quaternions $q = [q_1 \ q_2 \ q_3 \ q_4]^T$:

$$R(s) = \begin{bmatrix} q_1^2 + q_2^2 - q_3^2 - q_4^2 & 2(q_2q_3 - q_1q_4) & 2(q_2q_4 + q_1q_3) \\ 2(q_2q_3 + q_1q_4) & q_1^2 - q_2^2 + q_3^2 - q_4^2 & 2(q_3q_4 - q_1q_2) \\ 2(q_2q_4 - q_1q_3) & 2(q_3q_4 + q_1q_2) & q_1^2 - q_2^2 - q_3^2 + q_4^2 \end{bmatrix}. \tag{2}$$

The position vector r can be obtained by integrating the third column of the pose matrix R :

$$r(s) = \begin{bmatrix} X(s) \\ Y(s) \\ Z(s) \end{bmatrix} = \begin{bmatrix} 2 \int_0^s (q_2(\sigma)q_4(\sigma) + q_1(\sigma)q_3(\sigma)) d\sigma \\ 2 \int_0^s (q_3(\sigma)q_4(\sigma) - q_1(\sigma)q_2(\sigma)) d\sigma \\ \int_0^s (q_1^2(\sigma) - q_2^2(\sigma) - q_3^2(\sigma) + q_4^2(\sigma)) d\sigma \end{bmatrix}, \tag{3}$$

where σ denotes the integral variable.

Suppose the Young's modulus of the continuum robot is E , shear modulus is G , the diameter of backbone is d_e , the diameter of robot is d . The rate of change of $\Delta\varphi$ relative to s is defined as ω :

$$\omega = \lim_{\Delta s \rightarrow 0} \frac{\Delta\varphi}{\Delta s}. \tag{4}$$

The values of ω and q satisfy

$$\omega = \Gamma q', \tag{5}$$

where $q' = \frac{dq}{ds}$, and

$$\Gamma = 2 \begin{bmatrix} -q_2 & q_1 & q_4 & -q_3 \\ -q_3 & -q_4 & q_1 & q_2 \\ -q_4 & q_3 & -q_2 & q_1 \end{bmatrix}. \tag{6}$$

The total elastic potential energy, E_t , of the continuum robot includes elastic strain energy E_e and external force potential energy E_p . The variation in E_p represents the negative value of the external force virtual work, $\delta E_p = -\delta W$. When there is no obstacle constraint, the virtual work of external force is δW the virtual work of gravity δW_g . Thus, the variation of E_t is found as follows:

$$\delta E_t = \delta E_e - \delta W_g. \tag{7}$$

When the robot is in balance,

$$\delta E_t = 0. \tag{8}$$

The elastic strain energy can be obtained as follows:

$$E_e = \frac{1}{2} \int_0^L (k_x \omega_x^2 + k_y \omega_y^2 + k_z \omega_z^2) ds, \tag{9}$$

where (k_x, k_y, k_z) represents the bending stiffness around the coordinate axis.

$$k_x = E \frac{\pi d_e^4}{64} \quad k_y = E \frac{\pi d_e^4}{64} \quad k_z = G \frac{\pi d_e^4}{32}. \tag{10}$$

Substituting Eq. (5) into Eq. (9), the E_e can be rewritten as follows:

$$E_e = \frac{1}{2} \int_0^L (\boldsymbol{\omega}^T \mathbf{D} \boldsymbol{\omega}) ds, \tag{11}$$

where $\mathbf{D} = \text{diag}(k_x, k_y, k_z)$.

Consider the variation of Eq. (11),

$$\delta E_e = \int_0^L [(\mathbf{D} \boldsymbol{\omega})^T \delta \boldsymbol{\omega}] ds, \tag{12}$$

where $\delta \boldsymbol{\omega}$ can be obtained from Eq. (5)

$$\delta \boldsymbol{\omega} = \boldsymbol{\Gamma} \delta \mathbf{q}' - \boldsymbol{\Gamma}' \delta \mathbf{q}. \tag{13}$$

Suppose that \mathbf{q} at the N_i is $\mathbf{q}_i(s)$,

$$\mathbf{q}_i(s) = [q_{1,i} \ q_{2,i} \ q_{3,i} \ q_{4,i}]^T. \tag{14}$$

The forward difference scheme is used to calculate the derivative of $q_{k,i} (k = 1, 2, 3, 4)$:

$$q'_{k,i} = \frac{q_{k,i} - q_{k,i-1}}{2} \quad (i \geq 1). \tag{15}$$

The \mathbf{q} values at the N_{i-1} and N_i are combined into an 8 order array as follows:

$$\mathbf{q}_{i-1,i} = (\mathbf{q}_{i-1}^T \ \mathbf{q}_i^T)^T. \tag{16}$$

Then, \mathbf{q}_i and \mathbf{q}'_i can be expressed with $\mathbf{q}_{i-1,i}$ as follows:

$$\mathbf{q}_i = \boldsymbol{\Psi} \mathbf{q}_{i-1,i} \quad \mathbf{q}'_i = \boldsymbol{\Phi} \mathbf{q}_{i-1,i}, \tag{17}$$

where $\boldsymbol{\Psi}$ and $\boldsymbol{\Phi}$ are 4×8 matrices composed of 4 order zero matrix \mathbf{O}_4 and identity matrix \mathbf{E}_4 , respectively.

$$\boldsymbol{\Psi} = [\mathbf{O}_4 \ \mathbf{E}_4] \quad \boldsymbol{\Phi} = \frac{1}{l_r} [-\mathbf{E}_4 \ \mathbf{E}_4]. \tag{18}$$

From Eqs. (5), (13) and (17), the $\boldsymbol{\omega}$ and $\delta \boldsymbol{\omega}$ can be written as:

$$\boldsymbol{\omega} = \boldsymbol{\Gamma} \boldsymbol{\Phi} \mathbf{q}_{i-1,i} \quad \delta \boldsymbol{\omega} = \boldsymbol{\Gamma} \boldsymbol{\Phi} \delta \mathbf{q}_{i-1,i} - \boldsymbol{\Gamma}' \boldsymbol{\Psi} \delta \mathbf{q}_{i-1,i}. \tag{19}$$

Substituting Eq. (19) into Eq. (12), the strain energy of the robot can be discretized as follows:

$$\delta E_e = \sum_{i=1}^n (\mathbf{q}_{i-1,i}^T \boldsymbol{\Phi}^T \boldsymbol{\Gamma}_i^T \mathbf{D}^T) (\boldsymbol{\Gamma}_i \boldsymbol{\Phi} - \boldsymbol{\Gamma}'_i \boldsymbol{\Psi}) \delta \mathbf{q}_{i-1,i}. \tag{20}$$

Then, Eq. (20) can be abbreviated as follows:

$$\delta E_e = \sum_{i=1}^n (\mathbf{q}_{i-1,i}^T \mathbf{K}_i) \delta \mathbf{q}_{i-1,i}, \tag{21}$$

where

$$\mathbf{K}_i = \boldsymbol{\Phi}^T \boldsymbol{\Gamma}_i^T \mathbf{D}^T (\boldsymbol{\Gamma}_i \boldsymbol{\Phi} - \boldsymbol{\Gamma}'_i \boldsymbol{\Psi}). \tag{22}$$

The quaternions at the N_{i+1} are arranged into $4(n + 1)$ order arrays, \mathbf{q}_a , as follows:

$$\mathbf{q}_a = (\mathbf{q}_1^T \ \mathbf{q}_2^T \ \dots \ \mathbf{q}_{n+1}^T)^T. \tag{23}$$

The n matrices \mathbf{K}_i are arranged diagonally. The starting point of each unit and the ending point of the previous unit are the same. Thus, each matrix is moved by four rows and columns to the top and left. Then, the first four rows and columns of \mathbf{K}_i overlap with the last four rows and columns of \mathbf{K}_{i-1} , and the elements of the overlapping part are added one by one to form the $4(n + 1) \times 4(n + 1)$ order matrix \mathbf{K} . Subsequently, Eq. (21) can be expressed as follows:

$$\delta E_e = (\mathbf{q}_a^T \mathbf{K}) \delta \mathbf{q}_a. \tag{24}$$

When the robot is not considered to be in contact with the obstacle, the external force \mathbf{f}_c can be ignored. The virtual work of gravity force is found as follows:

$$\delta W_g = \int_0^L \mathbf{f}_g^T \delta \mathbf{r} ds, \tag{25}$$

where $\delta \mathbf{r}$ denotes the virtual displacement.

Applying the Simpson interpolation formula to Eq. (3) produces the following:

$$\begin{cases} X_i = \frac{l_r}{3} ((2q_{2,i-1} + q_{2,i})q_{4,i-1} + (2q_{2,i} + q_{2,i-1})q_{4,i} \\ \quad + (2q_{1,i-1} + q_{1,i})q_{3,i-1} + (2q_{1,i} + q_{1,i-1})q_{3,i}) + X_{i-1} \\ Y_i = \frac{l_r}{3} ((2q_{3,i-1} + q_{3,i})q_{4,i-1} + (2q_{3,i} + q_{3,i-1})q_{4,i} \\ \quad - (2q_{1,i-1} + q_{1,i})q_{2,i-1} - (2q_{1,i} + q_{1,i-1})q_{2,i}) + Y_{i-1} \\ Z_i = \frac{l_r}{3} (q_{1,i-1}^2 + q_{1,i-1}q_{1,i} + q_{1,i}^2 - q_{2,i-1}^2 - q_{2,i-1}q_{2,i} - q_{2,i}^2 \\ \quad - q_{3,i-1}^2 - q_{3,i-1}q_{3,i} - q_{3,i}^2 + q_{4,i-1}^2 + q_{4,i-1}q_{4,i} + q_{4,i}^2) + Z_{i-1} \end{cases}. \tag{26}$$

Then, \mathbf{r}_i can be expressed by \mathbf{U}_i as follows:

$$\mathbf{r}_i = \frac{1}{3} l_r \sum_{j=1}^i \mathbf{U}_j \mathbf{q}_{j-1,j}, \tag{27}$$

where

$$\mathbf{U}_i^{(1)} = \begin{bmatrix} 2q_{3,i-1} & 2q_{4,i-1} & q_{1,i} & q_{2,i} \\ -2q_{2,i-1} & -q_{1,i} & 2q_{4,i-1} & q_{3,i} \\ q_{1,i-1} + q_{1,i} & -(q_{2,i-1} + q_{2,i}) & -(q_{3,i-1} + q_{3,i}) & q_{4,i-1} + q_{4,i} \end{bmatrix}$$

$$U_i^{(2)} = \begin{bmatrix} 2q_{3,i} & 2q_{4,i} & q_{1,i-1} & q_{2,i-1} \\ -2q_{2,i} & -q_{1,i-1} & 2q_{4,i} & q_{3,i-1} \\ q_{1,i} & q_{2,i} & q_{3,i} & q_{4,i} \end{bmatrix}$$

$$U_i = [U_i^{(1)} \ U_i^{(2)}]. \tag{28}$$

Matrices U_i are arranged horizontally, where each matrix is moved by four columns to the left to form matrix U . Then, Eq. (25) can be abbreviated as follows:

$$\delta W_g = f_g^T U \delta q_a. \tag{29}$$

From Eqs. (24) and (29), the variation of E_t is as follows:

$$\delta E_t = (q_a^T K + f_g^T U) \delta q_a. \tag{30}$$

The following can be obtained from the robot balance condition Eq. (8):

$$q_a^T K + f_g^T U = 0. \tag{31}$$

Equation (31) is the unconstrained model of the robot.

2.2 Boundary conditions

When the robot runs along the pre-designed path, P_{Des} , it is necessary to add the boundary conditions of the robot’s endpoint position.

$$r_n = P_{Des} \tag{32}$$

2.3 Quasi-static model without obstacle constraints

Equations (31) and (32) constitute the unconstrained quasi-static model of the soft continuum robot.

$$f(q_a) = \begin{bmatrix} q_a^T K + f_g^T U \\ r_n - P_{Des} \end{bmatrix} = 0 \tag{33}$$

Using the least-squares method, the solution of Eq. (33) can be solved by LM optimization, and the LM algorithm flow is shown in Table 1, which could be implemented in MATLAB. In the LM algorithm, ϵ is a very small number, and α , β , μ and w are parameters, where $\alpha = 0.4$, $\beta = 0.55$, $\mu = 0.1$ and $w = 2$. Substituting the solution into Eq. (26) makes it possible to obtain the positions of each node, and the robot configuration can be obtained by interpolation fitting.

Table 1 LM algorithm flow

LM Algorithm
function $q_a = \text{LM}(f(q_a))$
$F(q_a) = \frac{1}{2} \sum_{i=1}^n f_i^2(q_a)$
$J(q_a) = \partial f(q_a) / \partial q_a$
while $F(q_a) > \epsilon$
$d(q_a) = -[J(q_a)^T J(q_a) + \mu I]^{-1} \nabla F(q_a)$
$m = 0$
while $F(q_a + \beta^m d(q_a)) < F(q_a) + \alpha \beta^m \nabla F(q_a) d(q_a)$
$m = m + 1$
end while
$d(q_a) = d(q_a) + \beta^m d(q_a)$
$\sigma = \frac{F(q_a + d(q_a)) - F(q_a)}{\nabla F(q_a)^T d(q_a) + \frac{1}{2} d(q_a)^T \nabla^2 F(q_a) d(q_a)}$
if $\sigma < 0.45$ $\mu = \mu w$ end if
if $\sigma > 0.75$ $\mu = \mu / w$ end if
if $0.45 \leq \sigma \leq 0.75$ $\mu = \mu$ end if
end while
end function
Output: q_a

2.4 Quasi-static model with obstacle constraints

A continuum robot is subjected to multiple types of constraints in the environment, mainly including the point, plane and surface constraints, where the surface constraints are the most complex. This study considered the cylinder constraint as an example, which is also the most common constraint in actual work, establishing a model with obstacle constraints.

A schematic diagram of a robot with the cylinder constraint is shown in Fig. 3. Because the actual calculation is for the configuration of the robot centerline, when considering environmental constraints, the diameter of the robot cannot be ignored. Suppose that the actual diameter of the constrained cylinder is w_1 , but calculated diameter w_2 is used as a variable, $w_2 = w_1 + d/2$. Part of the robot nodes is in contact with the constrained surface. Consider N_i as an example, which is simultaneously subjected to the force of gravity, f_g , and the force of the contact surface, f_c . The direction of f_c is the same as that of n_c , which is the normal vector of the cylinder at N_i .

When the robot is in contact with the constrained surface, the influence of f_c on the system energy needs to be considered. Suppose the set of nodes in contact with the constrained surface is Ω . The virtual work of the f_c is:

$$\delta W_c = \sum_{i \in \Omega} f_{c,i}^T \cdot \delta r_i. \tag{34}$$

The method of forming matrix $U_{c,i}$ is similar to the calculation of matrix U , but there are some difference.

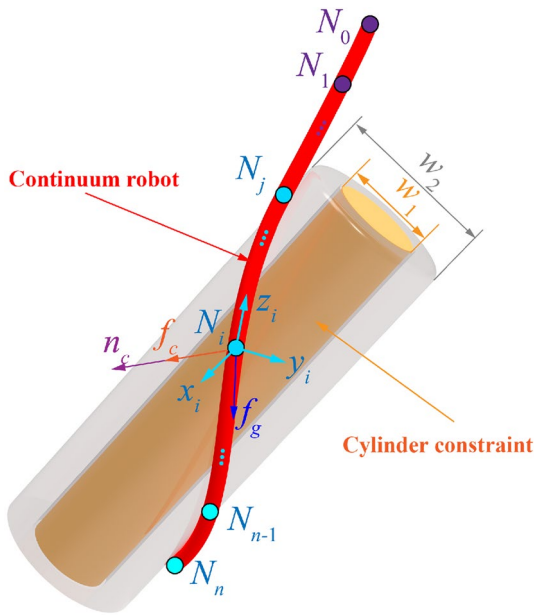


Fig. 3 Schematic of continuum robot with cylinder constraint

Matrices $U_{c,j}(j \leq i)$ are arranged horizontally, where each matrix is moved by four columns to the left to form matrix $U_{c,i}$. $U_{c,i}$ is a $3 \times 4(i + 1)$ order matrix, expanding $U_{c,i}$ to a $3 \times 4(n + 1)$ order matrix, as shown in follows:

$$U_{c,i} = [U_{c,i} \quad \mathbf{0}_{3 \times 4(n-i)}], \tag{35}$$

where $\mathbf{0}_{3 \times 4(n-i)}$ is $3 \times 4(n - i)$ order zero matrix.

Substituting Eq. (35) into Eq. (34), the virtual work of f_c is:

$$\delta W_c = \sum_{i \in \Omega} f_{c,i}^T U_{c,i} \delta q_a. \tag{36}$$

The variation of E_t needs to be adjusted to Eq. (37).

$$\delta E_t = \left(q_a^T K + f_g^T U + \sum_{i \in \Omega} f_{c,i}^T U_{c,i} \right) \delta q_a. \tag{37}$$

Then the balance equation is:

$$q_a^T K + f_g^T U + \sum_{i \in \Omega} f_{c,i}^T U_{c,i} = \mathbf{0}. \tag{38}$$

In addition, because the robot cannot cross the constraint surface, the configuration should also meet geometric constraints. The equation for a cylinder is denoted as:

$$c(X, Y, Z) = 0. \tag{39}$$

The normal vector n_c at any point on the cylinder is:

$$n_c = \left[\frac{\partial c}{\partial X} \quad \frac{\partial c}{\partial Y} \quad \frac{\partial c}{\partial Z} \right]^T. \tag{40}$$

From Eq. (2), the direction vector T at any node of the robot is:

$$T = \left[2(q_2 q_4 + q_1 q_3) \quad 2(q_3 q_4 - q_1 q_2) \quad q_1^2 - q_2^2 - q_3^2 + q_4^2 \right]^T. \tag{41}$$

When the robot is in contact with the constraint surface, $f_c \neq 0$ but $c(X, Y, Z) = 0$. In this situation, the direction of the robot is orthogonal to the surface, $n_c \cdot T = 0$. When the robot is detached from the constraint surface, $f_c = \mathbf{0}$, but $c(X, Y, Z) \neq 0$, and the value of $n_c \cdot T$ is uncertain. Thus, (41) is valid for any situations of the robot:

$$v_i = f_{c,i} \cdot c_i + f_{c,i} \cdot (n_c \cdot T_i) = 0. \tag{42}$$

Because the robot is always outside the constraint surface, any nodes N_i also needs to satisfy Eq. (43).

$$c(X_i, Y_i, Z_i) \geq 0 \tag{43}$$

Let v and c be sets found using of Eqs. (42) and (43) and composed of all the nodes in Ω , respectively.

$$v = \begin{bmatrix} v_{i1} \\ \vdots \\ v_{ih} \end{bmatrix} = \mathbf{0} \quad c = \begin{bmatrix} c_{i1} \\ \vdots \\ c_{ih} \end{bmatrix} \geq \mathbf{0} \quad (i1, \dots, ih) \in \Omega \tag{44}$$

Then, Eqs. (32), (38) and (44) constitute the constraint model of the soft continuum robot.

$$\begin{cases} q_a^T K + f_g^T U + \sum_{i \in \Omega} f_{c,i}^T U_{c,i} = \mathbf{0} \\ r_{n+1} - P_{Des} = \mathbf{0} \\ v = \mathbf{0} \\ c \geq \mathbf{0} \end{cases} \tag{45}$$

To solve Eq. (45) effectively, the Lagrange multiplier method is used to transform the inequality into an equality:

$$\rho c - \lambda^{(k)} = \mathbf{0}, \tag{46}$$

where ρ denotes the penalty factor, $\lambda^{(k)}$ is updated during each iteration, k represents the k_{th} iteration, and the updating criterion is as follows:

$$\lambda^{(k+1)} = \left| \rho c - \lambda^{(k)} \right|. \tag{47}$$

After the transformation, only the equality in Eq. (45) remains, and the the constraint model could be written as:

$$f(q_a) = \begin{bmatrix} q_a^T K + f_g^T U + \sum_{i \in \Omega} f_{c,i}^T U_{c,i} \\ r_{n+1} - P_{Des} \\ v \\ \rho c - \lambda^{(k)} \end{bmatrix} = \mathbf{0}. \tag{48}$$

Equation (48) could be solved by LM algorithm, as shown in Table 1.

When there is a constraint surface, firstly assuming that the obstacle constraint does not exist, and calculating the robot configuration. When the distance between a node and the axis of the obstacle cylinder is less than the radius of the cylinder, which means that the node passes through the obstacle, and the node is defined as an ‘‘interference node’’. Let Ω be the set of interference nodes, and calculate Eq. (48). If there are still exit some interference nodes in the calculation result, update Ω and Eq. (47) and calculate Eq. (48) again. Repeat this step until $\Omega = \emptyset$. The solving algorithm of soft continuum robot constraint model is shown in Table 2.

3 Results

3.1 Experiment preparation

At first, a continuum robot prototype driven by OAs was developed. Each section was driven by three airbags, and the lengths of the airbags could be varied by inflating or deflating them [46, 47]. The backbone of the robot was made up of an elastic rod. Based on the above structural

design, a prototype with 10 sections was developed. The robot was covered with a woven net. The experimental platform was composed of a continuum robot, a camera, and driving components, as illustrated in Fig. 4a. The drive component could be divided into two parts that were used for airbag inflation and deflation. The control system comprised upper computer (PC), lower computer (STM32), relays, and solenoid valves, as depicted in Fig. 4b. The upper computer control program was written in VC++ and communicated with the lower computer via Bluetooth. A group of relays and solenoid valves (30 each) were connected to an air compressor to inflate the airbags, with another group connected to a vacuum pump to deflate them, as depicted in Fig. 4(c). Installing pressure-regulating valves on the air compressors and vacuum pumps enabled precise control of the inflation/deflation speed. The camera, which could detect the space environment, was installed at the endpoint of the robot. An electromagnetic sensor (3D Guidance trakSTAR) could detect the position of robot endpoint. Only the inflation/deflation time is required to control the airbag length. The relationship between the airbag length and the inflation/deflation time was measured, as shown in Fig. 5. The parameters of the robot and algorithm are shown in Table 3.

For the continuum robot model, it was only possible to calculate the numerical solution, without being able to obtain an analytical solution. Therefore, the continuum robot model inevitably had calculation errors. Specifically, for point P in the task space, the solution obtained by solving the inverse kinematics model could be introduced to the forward kinematics model to obtain P', but P and P' were not completely coincident. The error in the Euclidean distance between P and P' was defined as the model error, e_m .

The number of elements had an important influence on e_m . In order to select the most appropriate number of elements. The e_m values and calculation times are depicted in Fig. 6. It is generally believed that a large number of elements produces a more model accurate model. However, the calculations in this study indicated that when the number of elements increased from 5 to 20, e_m gradually decreased, but when the number increased from 20 to 50, e_m gradually increased. This was because although additional elements could describe the robot more accurately, they also substantially increased the dimensionality and enhanced the nonlinearity of the equations, which reduced the accuracy of convergence. The calculation time is proportional to the number of units. When the number of elements was 20, the calculation time was 3.04 ms. Therefore, the influence of the model error and calculation time were comprehensively considered, and 20 was selected as the optimal number of model elements.

Table 2 Solving algorithm of soft continuum robot constraint model

Algorithm
$f(q_a) = \begin{bmatrix} q_a^T K + f_g^T U \\ r_n - P_{Des} \end{bmatrix} = \mathbf{0}$
$q_a = \text{LM}(f(q_a))$
Calculate interference nodes set Ω ;
while $\Omega \neq \emptyset$
for ($k = 0; k < K; k++$)
$f(q_a) = \begin{bmatrix} q_a^T K + f_g^T U + \sum_{i \in \Omega} f_{c,i}^T U_{c,i} \\ r_{n+1} - P_{Des} \\ v \\ \rho c - \lambda^{(k)} \end{bmatrix} = \mathbf{0}$
$q_a = \text{LM}(f(q_a));$
$\lambda^{(k+1)} = \rho c - \lambda^{(k)} ;$
end for
Update Ω ;
end while
Output: q_a

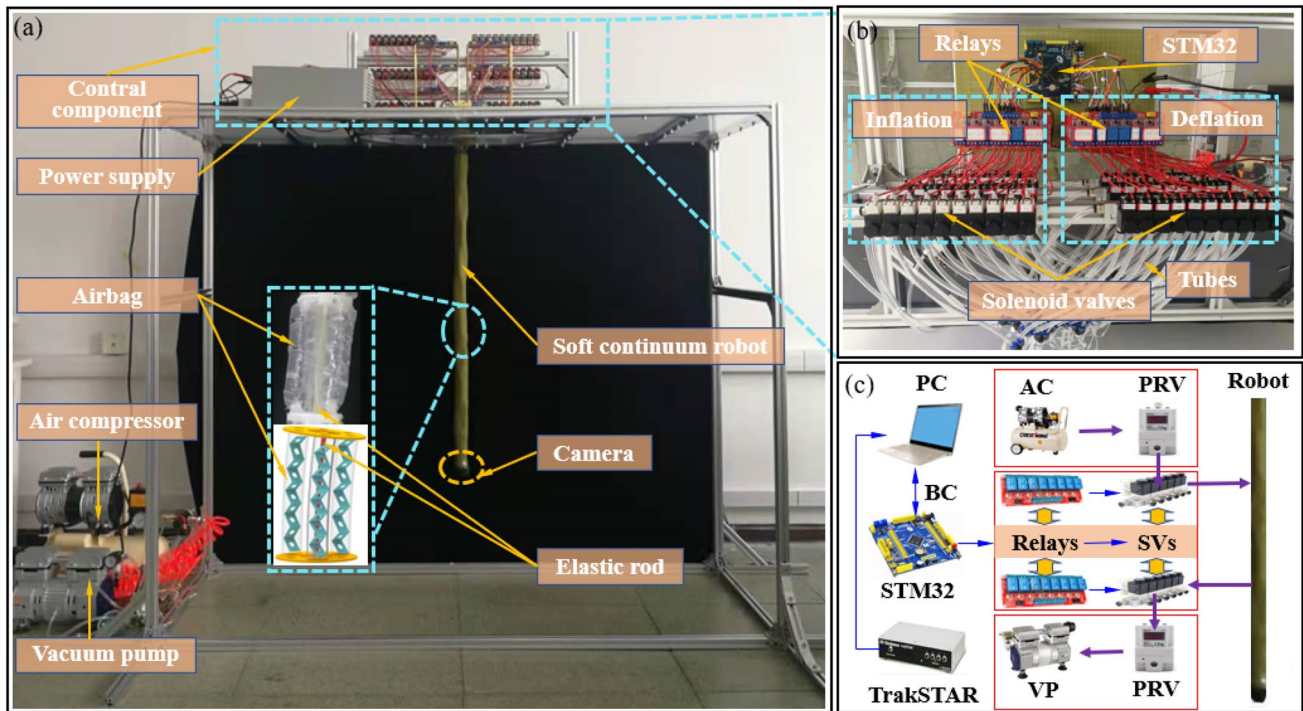


Fig. 4 a Illustration of the experimental platform. b Schematic of control components. c Flowchart of control system. The thin blue line represents the direction of the electrical signal transmission, and the

thick purple line represents the direction of the airflow. BC bluetooth communication, AC air compressor, PRV pressure-regulating valve, SV solenoid valve, VP vacuum pump (Color figure online)

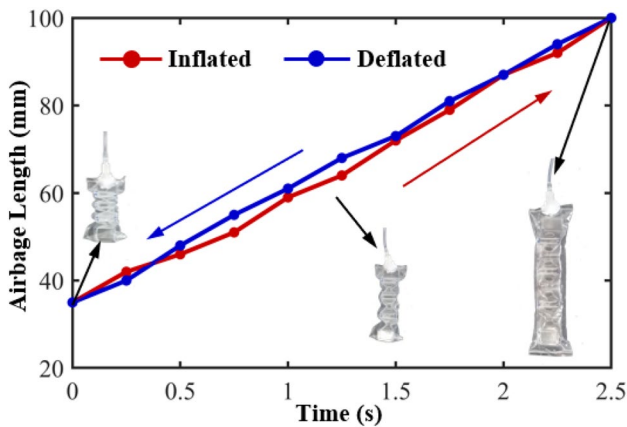


Fig. 5 Variation in the length of the airbag under the conditions of inflation (red line) and deflation (blue line). The maximum length of a single airbag is 100 mm, and minimum length is 35 mm (Color figure online)

3.2 Experiment 1—moving to target points

Based on the unconstrained model Eq. (33), an experiment involving “moving to target points” was firstly conducted

Table 3 Robot and algorithm parameters

Symbol	Meaning	Value
L	Robot length	1000 mm
d	Robot diameter	40 mm
d_e	Elastic rod diameter	2.5 mm
E	Young’s modulus	6.2 MPa
G	Shear modulus	2.4 Mpa
f_g	Robot gravity	0.004 N/mm
ρ	Penalty factor	2
$\lambda^{(0)}$	Multiplier vector initial value	$\mathbf{0}$ (zero vector)
K	Number of iterations allowed	10

The bold symbols are vectors

with five target points. The positions of the target points were introduced into the model as boundary conditions, and the calculated results were applied to control the robot to move to the target points. The endpoint position was measured with an electromagnetic sensor and output to the computer. Comparisons between the simulation and experimental results are depicted in Fig. 7. In the experiment, we placed a ping pong ball at the target point to clarify the

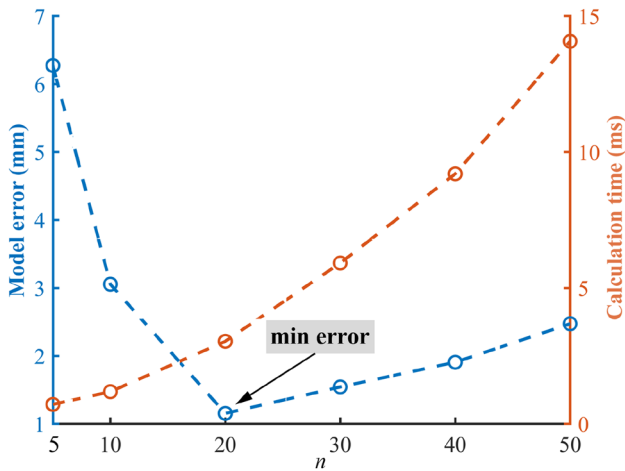


Fig. 6 Model error and calculation time values with different numbers of elements

location of the target points. The simulation of the robot configurations matches the experimental results well.

The ratio of the Euclidean distance between the actual position of the endpoint and the target point to the length of the robot is defined as the error. We compared the control effect of robot with other two commonly used model—piecewise constant curvature method and Cosserat rod method. The proposed model, piecewise constant curvature method and Cosserat rod method are named model 1, 2 and 3, respectively. Figure 8 shows the errors of the robot endpoints corresponding to different target points. The errors, which named Errors 1, 2 and 3, are 2.02%, 2.97% and 2.54% of the model 1, 2 and 3, respectively.

3.3 Experiment 2—complex trajectory tracking (“SIA”)

Specific path tasks must often be accomplished for a soft continuum robot, which can be discretized into a series of target points. Thus, it was only necessary to “moving to target points”, which could be achieved by the proposed model, as demonstrated in experiment 1. At First, The paths for the

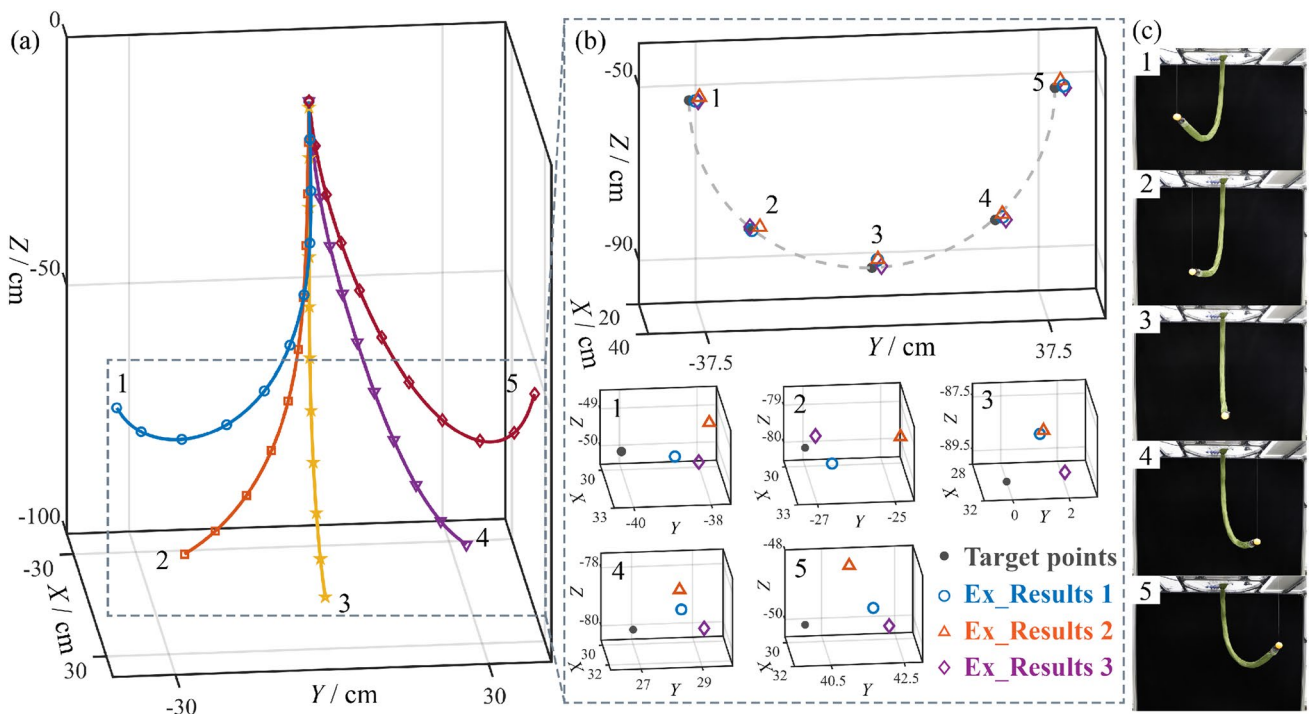


Fig. 7 **a** Simulation results for robot configurations with different target points. **b** Comparison of the simulation and the experimental results for the endpoint positions. Ex_Results 1, 2 and 3 are the experimental results of model 1, 2 and 3. **c** Experimental photos of the proposed model

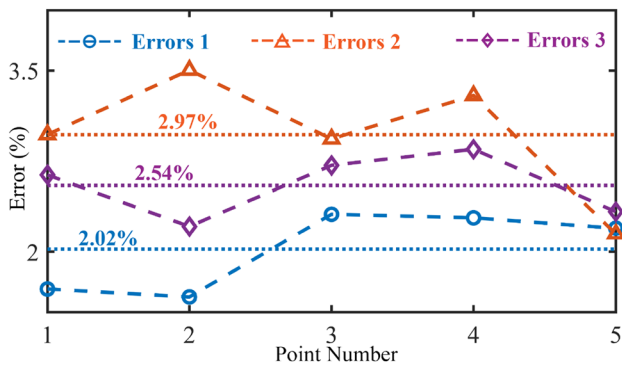


Fig. 8 Endpoints errors of different modelling methods

three letters “SIA” were defined, with “S” and “A” discretized into 10 points, and “I” discretized into 5 points. Then, all the points were calculated. The theoretical predicted values and experimental results of the robot configurations and paths are depicted in Fig. 9, and the endpoint position errors are shown in Fig. 10. The average position errors of the model 1, 2, and 3 are 2.07%, 3.05% and 2.54%, respectively.

3.4 Experiment 3—contact with obstacles

Continuum robots inevitably encounter obstacle constraints when moving in cluttered environments, and such constraints typically have a serious impact on robot motion. Based on the proposed obstacle constraint model for continuum robots, two experiments were conducted with spatial cylindrical constraints. First, constrained cylinder and target points were defined in a three-dimensional space. The proposed model was then used to calculate and control the motion of the robot, which needed to bypass the obstacles to reach the target points. Two sets of experiments (E3.1 and E3.2) were conducted to define two different sets of cylindrical constraints and target points, respectively. The axis of the space cylinder in the first and second sets of experiments are $-1.42y + z + 37.79 = 0$ and $1.42y + z + 37.79 = 0$, respectively. The radius is 7 cm. The simulation and experimental results of the robot configurations are shown in Fig. 11, where it can be observed that the simulation and experimental results are considerably close. The endpoint position errors when reaching the target points in the first and second

sets of experiments were 2.386% and 2.262%, respectively, and the average value of the error was 2.446%, as depicted in Fig. 12.

3.5 Discussion

Three sets of experiments were conducted to validate the proposed model. For the case without obstacle constraints, the mean errors of the robot endpoints corresponding to the proposed model, piecewise constant curvature method and Cosserat rod method, are 2.045%, 3.01%, and 2.54%, respectively. Compared with the other two models, the proposed model has higher accuracy. For the case with an obstacle constraint, the mean error of the robot endpoint was 2.446%. According to the experimental results, the proposed model could predict the robot configuration and control the robot endpoint move to the target points well. When there was an obstacle constraint, the obstacle had an important influence on the robot configuration, which proved the necessity of the theoretical modeling in this study.

4 Conclusion

This work investigated a variable-curvature modelling method of soft continuum robots based on the principle of virtual work, and an obstacle constraint model was established. The proposed model could be used for motion control effectively.

The proposed model could be used for soft continuum robot design analysis and path following, particularly in the environments with obstacle constraints. Feedforward control based on the proposed model would eliminate the need for an additional sensor system to measure the real-time configuration of the robot, which is important for extending the range of applications of soft continuum robots and interacting safely with complex environments.

The proposed method is applicable to the case where the constrained surface parameters are known. In future work, we will try to combine the method of this paper with vision, collecting constraint information through machine vision to build a model of the constrained surface parameters, and then the model could be applied to a strange environment.

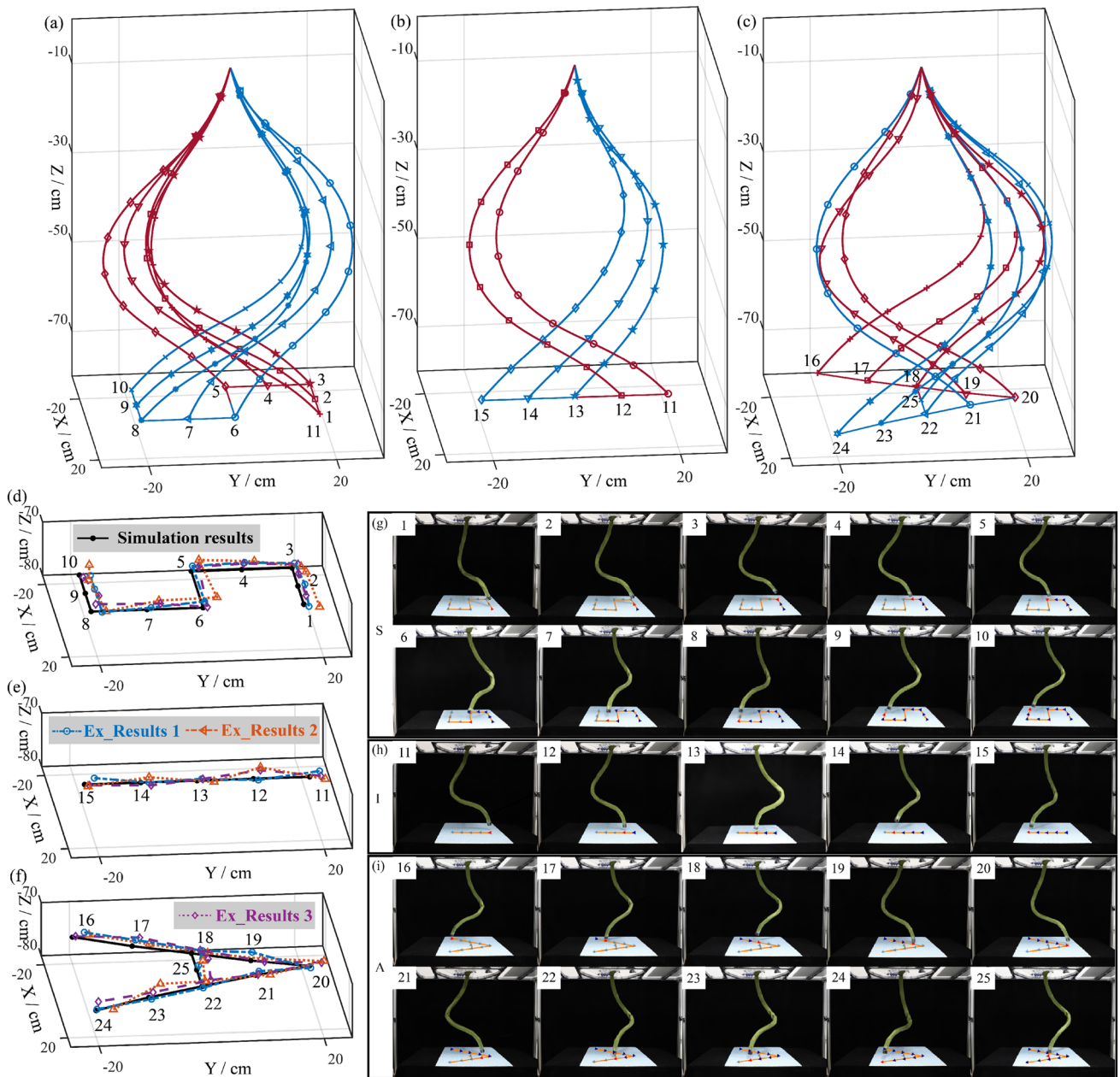


Fig. 9 a–c Show the soft continuum robot simulation configurations for “S”, “I”, and “A”, respectively. d–f Show the simulation and experimental paths for the endpoints of “S”, “I” and “A”, respectively. g–i Show the experimental photographs of the paths for “S”, “I”, and “A”, respectively. Ex_Results 1, 2 and 3 are the experimental results

of model 1, 2 and 3, respectively. In g–i, the red arrows indicate the positions being passed, dark blue arrows indicate the positions that have been passed, and the light blue arrows indicate the positions that have not yet been passed (Color figure online)

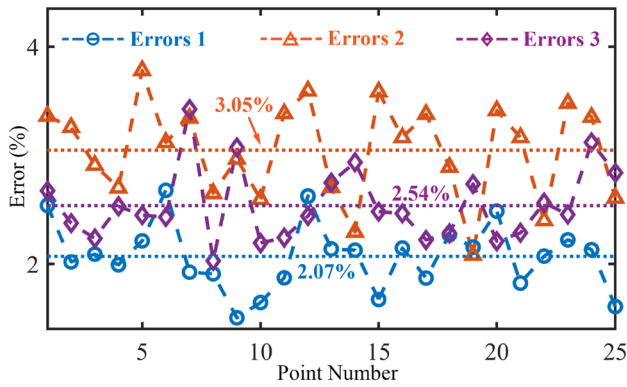


Fig. 10 Errors for endpoints of complex paths—“SIA”

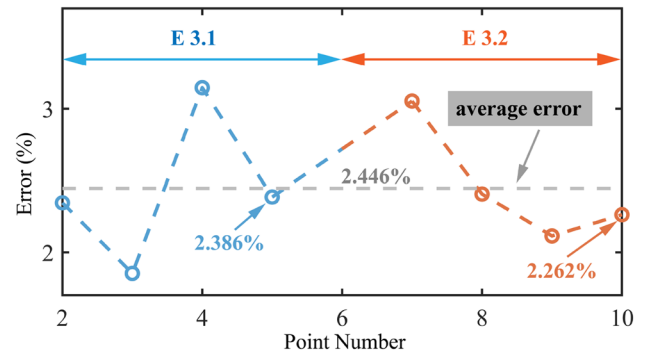


Fig. 12 Errors for endpoints with cylindrical obstacle constraints

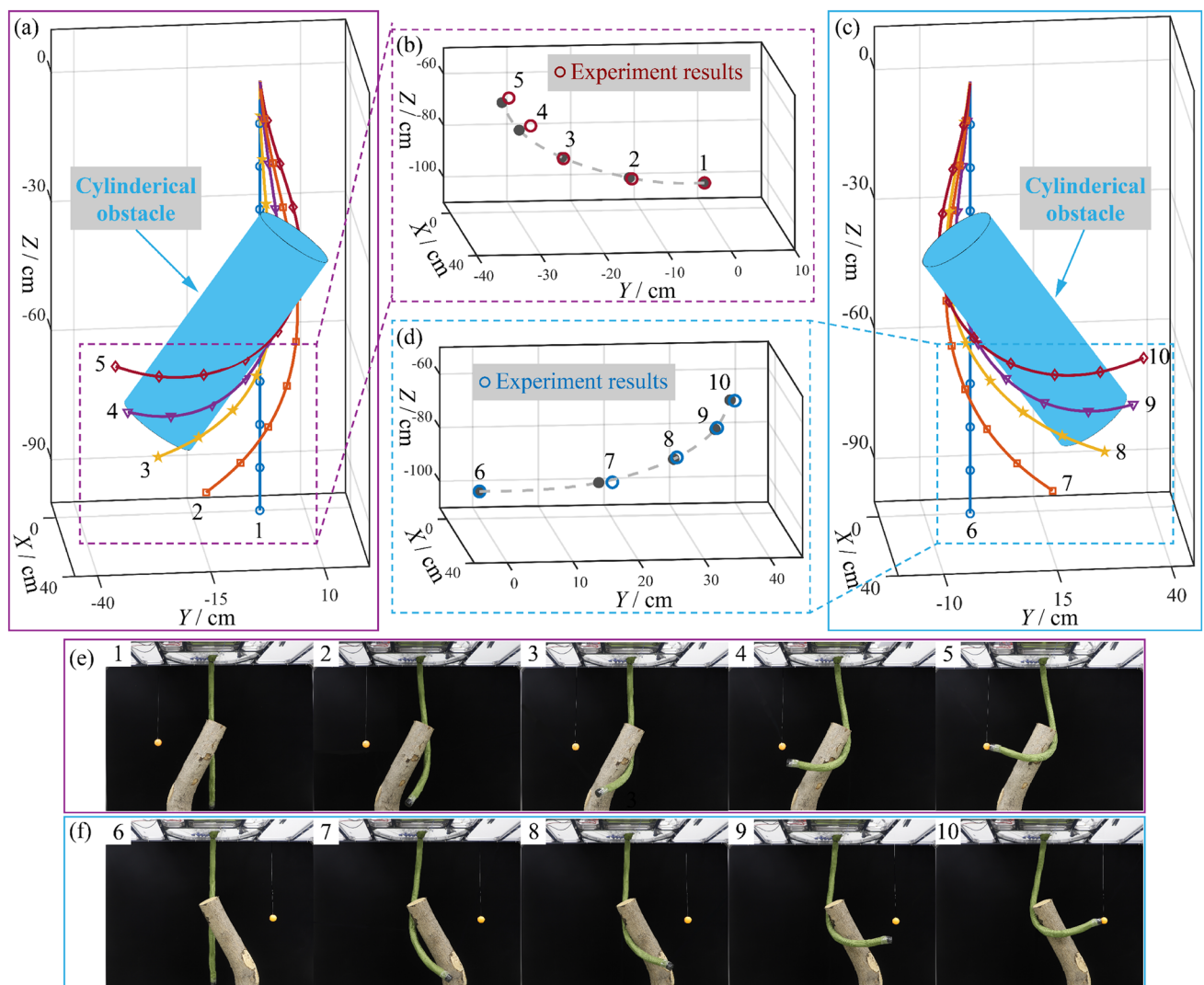


Fig. 11 a, c Are depict simulation results for the configuration of the robot with an obstacle in the first and second sets, respectively. In a, point 1 represents the initial state of the robot, and when the robot moves to points 2–5 it makes contact with the obstacle (cylindrical constraint). In c, point represents the initial state of the robot, and

when the robot moves to points 7–10 it makes contact with the obstacle. b, d Show the comparisons between the theoretical and experimental results in the first and second sets, respectively. e, f Show the experimental photographs for the first and second sets, respectively

Acknowledgements The work was supported by National Natural Science Foundation of China (51975566, U1908214), National Key R&D Program of China (2018YFB1304600), and CAS Interdisciplinary Innovation Team (JCTD-2018-11).

Funding The funding has been received from National Natural Science Foundation of China with Grant no. 51975566.

Data availability The data that support the findings of this study are available from the corresponding author, upon reasonable request.

Declarations

Conflict of interest The authors declare that they have no conflict of interest.

References

- Rus D, Tolley MT (2015) Design, fabrication and control of soft robots. *Nature* 521(7553):467–475
- Hwang G, Park J, Cortes D, Hyeon K, Kyung K (2022) Electro-adhesion-based high-payload soft gripper with mechanically strengthened structure. *IEEE Trans Ind Electron* 69(1):642–651
- Li H, Yao J, Liu C, Zhou P, Xu Y, Zhao Y (2018) A bioinspired soft swallowing robot based on compliant guiding structure. *Soft Robot* 7(4):491–499
- Hawkes EW, Blumenschein LH, Greer JD, Okamura AM (2017) A soft robot that navigates its environment through growth. *Sci Robot* 2(8):3028
- Pang G, Yang G, Heng W, Ye Z, Huang X, Yang H, Pang Z (2021) CoboSkin: soft robot skin with variable stiffness for safer human-robot collaboration. *IEEE Trans Ind Electron* 68(4):3303–3314
- Laschi C, Mazzolai B, Cianchetti M (2016) Soft robotics: technologies and systems pushing the boundaries of robot abilities. *Sci Robot* 1(1):3690
- Joseph DG, Tania KM, Allison MO, Elliot WH, Soft A (2019) Steerable continuum robot that grows via tip extension. *Soft Robot* 6(1):95–108
- Kim Y, Parada GA, Liu S, Zhao X (2019) Ferromagnetic continuum robots. *Sci Robot* 4(33):7329
- Shabana AA (2018) Continuum-based geometry/analysis approach for flexible and soft robotic systems. *Soft Robot* 5(5):613–621
- Renda F, Giorelli M, Calisti M, Cianchetti M (2014) Dynamic model of a multibending soft robot arm driven by cables. *IEEE Trans Robot* 30(5):1–14
- Renda F, Boyer F, Dias J, Seneviratne L (2018) Discrete Cosserat approach for multisection soft manipulator dynamics. *IEEE Trans Robot* 34(6):1518–1533
- Catalano MG, Grioli G, Farnioli E, Serio A, Piazza C, Bicchi A (2014) Adaptive synergies for the design and control of the Pisa/IIT SoftHand. *Int J Robot Res* 33(5):768–782
- Yang H, Xu M, Li W, Zhang S (2019) Design and implementation of a soft robotic arm driven by SMA coils. *IEEE Trans Ind Electron* 66(8):6108–6116
- Rone WS, Ben-Tzvi P (2014) Continuum robot dynamics utilizing the principle of virtual power. *IEEE Trans Robot* 30(1):275–287
- Kang R, Branson DT, Zheng T, Guglielmino E, Caldwell DG (2013) Design, modeling and control of a pneumatically actuated manipulator inspired by biological continuum structures. *Bioinspir Biomim* 8(3):036008
- Kang R, Guo Y, Chen L, Branson DT, Dai JS (2016) Design of a pneumatic muscle based continuum robot with embedded tendons. *IEEE-ASME Trans Mechatron* 22(2):751–761
- Yang J, Peng H, Zhou W, Zhang J, Wu Z (2021) A modular approach for dynamic modeling of multisegment continuum robots. *Mech Mach Theory* 165:104429
- Webster RJ, Jones BA (2010) Design and kinematic modeling of constant curvature continuum robots: a review. *Int J Robot Res* 29(13):1661–1683
- Yuan H, Zhou L, Xu W (2019) A comprehensive static model of cable-driven multi-section continuum robots considering friction effect. *Mech Mach Theory* 135:130–149
- Burgner-Kahrs J, Rucker DC, Choset H (2015) Continuum robots for medical applications: a survey. *IEEE Trans Robot* 31(6):1261–1280
- Yang HD, Asbeck AT (2020) Design and characterization of a modular hybrid continuum robotics manipulator. *IEEE-ASME Trans Mechatron* 25(6):2812–2823
- Misher MK, Samantaray AK, Chakraborty G, Jain A, Pathak P, Merzouki R (2019) Dynamic modelling of an elephant trunk like flexible bionic manipulator. In: Proceedings of the ASME 2019 international mechanical engineering congress and exposition (IMECE)
- Greer JD, Morimoto TK, Okamura AM, Hawkes EW (2017) Series pneumatic artificial muscles (SPAMs) and application to a soft continuum robot. In: 2017 IEEE international conference on robotics and automation (ICRA). IEEE, pp 5503–5510
- Greer JD, Morimoto TK, Okamura AM, Hawkes EW, Soft A (2019) Steerable continuum robot that grows via tip extension. *Soft Robot* 6(1):95–108
- Marchese AD, Rus D (2015) Design, kinematics, and control of a soft spatial fluidic elastomer manipulator. *Int J Robot Res* 35(7):840–869
- Webster RJ, Romano JM, Cowan NJ (2009) Mechanics of pre-curved-tube continuum robots. *IEEE Trans Robot* 25(1):67–78
- Rucker DC, Webster RJ, Chirikjian GS (2010) Equilibrium conformations of concentric-tube continuum robots. *Int J Robot Res* 29(10):1263–1280
- Escande C, Chettibi T, Merzouki R, Coelen V, Pathak PM (2014) Kinematic calibration of a multisection bionic manipulator. *IEEE-ASME Trans Mechatron* 20(2):663–674
- Gong Z, Fang X, Chen X, Cheng J, Xie Z, Liu J, Chen B, Yang H, Kong S, Hao Y, Wang T, Yu J, Wen L (2020) A soft manipulator for efficient delicate grasping in shallow water: modeling, control, and real-world experiments. *Int J Robot Res* 40(1):449–469
- Yang C, Geng S, Walker I, Branson DT, Liu J, Dai J, Kang R (2020) Geometric constraint-based modeling and analysis of a novel continuum robot with shape memory alloy initiated variable stiffness. *Int J Robot Res* 39(14):1620–1634
- Godage S, Medrano-Cerda GA, Branson DT, Guglielmino E, Caldwell DG (2015) Modal kinematics for multisection continuum arms. *Bioinspir Biomim* 10(3):035002
- Gonthina PS, Kapadia AD, Godage IS, Walker ID (2019) Modeling variable curvature parallel continuum robots using Euler curves. In: 2019 International conference on robotics and automation (ICRA), pp 1679–1685
- Singh I, Amara Y, Melingui A, Mani Pathak P, Merzouki R (2018) Modeling of continuum manipulators using pythagorean hodograph curves. *Soft Robot* 5(4):425–442
- Bieze TM, Largilliere F, Kruszewski A, Zhang Z, Merzouki R, Duriez C (2018) Finite element method-based kinematics and closedloop control of soft, continuum manipulators. *Soft Robot* 5(3):348–364
- Huang X, Zou J, Gu G (2021) Kinematic modeling and control of variable curvature continuum robots. *IEEE-ASME Trans Mechatron* 26(6):3175–3185

36. Godage S, Wirz R, Walker ID, Webster RJ (2015) Accurate and efficient dynamics for variable-length continuum arms: a center of gravity approach. *Soft Robot* 2(3):96–106
37. Coevoet E, Escande A, Duriez C (2017) Optimization-based inverse model of soft robots with contact handling. *IEEE Robot Autom Lett* 2(3):1413–1419
38. Pall E, Sieverling A, Brock O (2018) Contingent contact-based motion planning. In: *IEEE/RSJ international conference on intelligent robots and systems (IROS)*, pp 6615–6621
39. Sieverling A, Eppner C, Wolff F, Brock O (2017) Interleaving motion in contact and in free space for planning under uncertainty. In: *IEEE/RSJ international conference on intelligent robots and systems (IROS)*, pp 4011–4073
40. Zhang Z, Dequidt J, Back J, Liu H, Duriez C (2019) Motion control of cable-driven continuum catheter robot through contacts. *IEEE Robot Autom Lett* 4(2):1852–1859
41. Yip MC, Camarillo DB (2014) Model-less feedback control of continuum manipulators in constrained environments. *IEEE Trans Robot* 30(4):880–889
42. Chen Y, Wang L, Galloway K, Godage I, Simaan N, Barth E (2021) Modal-based kinematics and contact detection of soft robots. *Soft Robot* 8(3):298–309
43. DellaSantina C, Katzschmann RK, Bicchi A, Rus D (2020) Model-based dynamic feedback control of a planar soft robot: trajectory tracking and interaction with the environment. *Int J Robot Res* 39(4):490–513
44. Greer D, Blumenschein LH, Alterovitz R, Hawkes EW, Okamura AM (2020) Robust navigation of a soft growing robot by exploiting contact with the environment. *Int J Robot Res* 39(14):1724–1738
45. Merzouki R, Samantaray AK, Pathak PM, Ould Bouamama B (2013) Rigid body, flexible body and micro electromechanical systems. In: *Intelligent mechatronic systems: modelling, control and diagnosis*. Springer London, UK, pp 313–315
46. Li S, Vogt DM, Rus D, Wood RJ (2017) Fluid-driven origami-inspired artificial muscles. In: *Proceedings of the National Academy of Sciences of the United States of America (PNAS)*, pp 13132–13137
47. Lee G, Rodrigue H (2019) Origami-based vacuum pneumatic artificial muscles with large contraction ratios. *Soft Robot* 6(1):109–117

Publisher's Note Springer Nature remains neutral with regard to jurisdictional claims in published maps and institutional affiliations.

Springer Nature or its licensor (e.g. a society or other partner) holds exclusive rights to this article under a publishing agreement with the author(s) or other rightsholder(s); author self-archiving of the accepted manuscript version of this article is solely governed by the terms of such publishing agreement and applicable law.